PROCEEDINGS OF SPIE

SPIEDigitalLibrary.org/conference-proceedings-of-spie

Laboratory-based phase and absorption tomography for micro-imaging of annual layers in human tooth cementum, paraffin-embedded nerve and zebrafish embryo

Migga, Alexandra, Schulz, Georg, Rodgers, Griffin, Osterwalder, Melissa, Tanner, Christine, et al.

Alexandra Migga, Georg Schulz, Griffin Rodgers, Melissa Osterwalder, Christine Tanner, Holger Blank, Iwan Jerjen, Phil Salmon, William Twengström, Mario Scheel, Timm Weitkamp, Christian M. Schlepütz, Jan S. Bolten, Jörg Huwyler, Gerhard Hotz, Srinivas Madduri, Bert Müller, "Laboratory-based phase and absorption tomography for micro-imaging of annual layers in human tooth cementum, paraffin-embedded nerve and zebrafish embryo," Proc. SPIE 11840, Developments in X-Ray Tomography XIII, 118400T (7 October 2021); doi: 10.1117/12.2597926

SPIE.

Event: SPIE Optical Engineering + Applications, 2021, San Diego, California, United States

Laboratory-based phase and absorption tomography for micro-imaging of annual layers in human tooth cementum, paraffin-embedded nerve and zebrafish embryo

Alexandra Migga[a,b], Georg Schulz[a,c,*], Griffin Rodgers[a,b], Melissa Osterwalder[a,b], Christine Tanner[a,b], Holger Blank[d], Iwan Jerjen[e], Phil Salmon[f], William Twengström[g], Mario Scheel[h], Timm Weitkamp[h], Christian Matthias Schlepütz[i], Jan Stephan Bolten[j], Jörg Huwyler[j], Gerhard Hotz[k,l], Srinivas Madduri[a,m,n], and Bert Müller[a,b]

[a]Biomaterials Science Center, Department of Biomedical Engineering, University of Basel, 4123 Allschwil, Switzerland; [b]Biomaterials Science Center, Department of Clinical Research, University Hospital Basel, 4031 Basel, Switzerland; [c]Core Facility Micro- and Nanotomography, Department of Biomedical Engineering, University of Basel, 4123 Allschwil, Switzerland; [d]Carl Zeiss Microscopy GmbH, 73447 Oberkochen, Germany; [e]Gloor Instruments AG, 8302 Kloten, Switzerland; [f]Bruker micro CT, 2550 Kontich, Belgium; [g]Exciscope AB, 164 40 Kista, Sweden; [h]Synchrotron Soleil, 91192 Gif-sur-Yvette, France; [i]Swiss Light Source, Paul Scherrer Institut, 5232 Villigen, Switzerland; [j]Pharmaceutical Technology, Department of Pharmaceutical Sciences, University of Basel, 4056 Basel, Switzerland; [k]Natural History Museum of Basel, Anthropological Collection, 4501 Basel, Switzerland; [l]Integrative Prehistory and Archaeological Science, University of Basel, 4055 Basel, Switzerland; [m]Department of Surgery, University of Geneva, 41205 Geneva; [n]Department of Plastic, Reconstructive, Aesthetic and Hand Surgery, University Hospital Basel, 4031 Basel, Switzerland

ABSTRACT

Synchrotron radiation-based tomography yields the micro-anatomical features in human and animal tissues without physical slicing. Recent advances in instrumentation have made laboratory-based phase tomography feasible. We compared the performance of three cutting-edge laboratory systems benchmarked by synchrotron radiation-based tomography for three specimens. As an additional criterion, the user-friendliness of the three microtomography systems is considered. The three tomography systems—SkyScan 2214 (Bruker-microCT, Kontich, Belgium), Xradia 620 Versa (Zeiss, Oberkochen, Germany) and the prototype of Exciscope (Stockholm, Sweden)—were given 36 hours to measure three medically relevant specimens—archaeological human tooth, porcine nerve and zebrafish embryo. The obtained datasets were registered to the benchmark synchrotron radiation-based tomography from the same specimens and to the SkyScan 1275 and phoenix nanotom m® laboratory systems to characterize the development during the last decade. The next-generation laboratory-based microtomography almost reached the quality of synchrotron-radiation facilities with respect to spatial and density resolution, as indicated by the visualization of the medically relevant micro-anatomical features. The Exciscope prototype and the SkyScan 2214 demonstrated the complementarity of phase information by imaging the eyes of the zebrafish embryo. The Xradia 620 Versa enabled the three-dimensional visualization of the 2 to 3 µm-thin annual layers in tooth cementum. The data of the Exciscope prototype with the high photon flux from the liquid metal source from Excillum (Kista, Sweden) showed the spiral nature of the myelin sheaths in the porcine nerve. The SkyScan 2214, the most effortable among the three next-generation systems evaluated, was well suited to visualize the wealth of anatomical features in the zebrafish embryo.

Keywords: Phase-contrast tomography, image registration, X-ray microscopy, phase retrieval, tooth cementum, porcine nerve, zebrafish larvae, spatial and density resolution

*georg.schulz@unibas.ch; phone +41 61 207 5430; bmc.unibas.ch

Developments in X-Ray Tomography XIII, edited by Bert Müller
Ge Wang, Proc. of SPIE Vol. 11840, 118400T · © 2021 SPIE
CCC code: 0277-786X/21/$21 · doi: 10.1117/12.2597926

1. INTRODUCTION

Hard X-ray microtomography is a three-dimensional imaging technique that allows for the quantitative evaluation of microstructures in *post mortem* tissues [1]. Advanced instrumentation is applied for myriad scientific purposes including the characterization of annual layers in cementum of human teeth [2], the visualization of paraffin-embedded nerves [3], and the anatomical analysis of zebrafish embryos [4]. Traditionally, the highest density and spatial resolutions have been achievable at synchrotron radiation facilities with restricted user access. Laboratory-based systems have been improved substantially by incorporating phase-contrast capabilities and X-ray detector optics [5]. With the increasing number of such systems on the market, a detailed comparison is needed to understand performance of these next-generation scanners with respect to other available laboratory systems and dedicated microtomography beamlines at synchrotron radiation facilities. To this end, the performance of three cutting-edge laboratory-based tomography systems employing absorption and phase contrast modes were compared for the above-mentioned scientific applications. The common volumes extracted from datasets were three-dimensionally registered to synchrotron radiation-based micro computed tomography from the TOMCAT beamline at the Swiss Light Source (Paul Scherrer Institute, Villigen, Switzerland) and the ANATOMIX beamline at the Synchrotron SOLEIL (Gif-Sur-Yvette, France) and evaluated with respect to spatial resolution and contrast. In addition, the user friendliness of the three next-generation scanners was appraised in detail.

1.1 Laboratory-based phase-contrast X-ray tomography

Conventional X-ray tomography used in medicine relies on absorption contrast, well suitable for imaging of hard tissues. Soft tissue imaging usually requires appropriate staining. As alternative, one can take advantage of phase contrast modes to visualize the tissues consisting of light elements together with hard tissue components including teeth, bone, and plaque [6], which is especially demanding for attenuation-contrast X-ray tomography. As the X-ray beam passes through condensed matter, it exhibits both absorption and, with sufficient beam coherence, a phase shift [7]. For soft tissues, the linear absorption coefficient is three orders of magnitudes lower than the related coefficient for the phase shift [8]. Thus, for the majority of medically relevant hard X-ray imaging of tissues in health and disease, phase-contrast methods are preferred [8]. Several phase tomography approaches have been evaluated for soft tissue imaging [6, 8-12]. Single-distance propagation-based approaches are often the simplest to implement and generally offer the best spatial resolution. Therefore, these systems are frequently used at micro- and nanotomography beamlines of synchrotron radiation facilities and are being implemented in sophisticated laboratory-based microtomography systems.

High-resolution microtomography is more and more often referred to as virtual histology because it extends the anatomical information from conventional histological sections to the third dimension [13, 14]. Virtual histology yields anatomical information without physical slicing. The spatial resolution is equal in the three orthogonal directions, a distinct feature compared to serial sectioning and essential for the anatomical context, e.g. nervous tissue, as well as simple and fast data acquirement for much larger samples [5, 13]. Using nanoholotomography, one can even reach a spatial resolution beyond the optical limit given by the optical means employed to image the histological slices [15]. Such measurements, however, suffer from the restricted access of the synchrotron radiation facilities. The purchase of beamtime is only common for industrial research, and research proposal can only be submitted twice a year, which leads to substantial delays and the focus on a smaller number of priority samples. As an alternative, several research teams use virtual histology based on laboratory-based microtomography systems. The obtained results, however, are generally compromised with respect to the data from synchrotron radiation-based systems. The gap between the laboratory- and synchrotron radiation-based tomography data, clearly obvious a decade ago [16], is becoming narrower and narrower, see e.g. [17, 18] with only minor differences in image quality [5, 13, 19]. These advances in the laboratory-based approaches have motivated our team to evaluate the cutting-edge instrumentation with the goal to directly compare the tomographic imaging of selected, medically relevant scientific questions related to the annual layers in human tooth cementum, to the three-dimensional representation of paraffin-embedded porcine nerves, and to the cellular anatomy of zebrafish larvae. The acquisition of the necessary radiographs from the three selected specimens and their reconstruction was restricted to a period of 36 hours per advanced instrument in order to guarantee comparability and to have a reasonable timeframe for future experiments. It should be noted that while longer experiments could yield substantially better deliverables, the 36-hour period was selected to resemble the standard user experience. As a benchmark, the three specimens were imaged, prior to the measurements with the advanced instrumentation, at the tomography setups of the beamlines TOMCAT or ANATOMIX. In order to validate the progress in the imaging of the three selected specimens, the laboratory-based systems SkyScan 1275 (Bruker microCT, Kontich, Belgium) and nanotom m® (Waygate Technologies, phoenix|x-ray, Wunstorf, Germany) were included into the comparison. The six datasets per specimen were three-dimensionally registered to segment the common volume for the qualitative and quantitative comparison of the image quality.

1.2 Tooth root cementum – a lifelong growing, mineralized tissue

Tooth cementum is a mineralized tissue that exists in vertebra teeth and covers the entire surface of the tooth root, belonging functionally to its anchor, the periodontium. In contrast to bone, this avascular complex is independent of regular remodeling, thus, expands lifelong with location-dependent growth rates [20, 21]. For humans, the homogeneous structure reveals about 3 µm-thin incremental layers as originally found in optical micrographs of thin tooth slices [22]. These incremental layers were recently detected using synchrotron radiation-based microtomography [2]. Our team is currently evaluating data of an entire tooth collected during a beamtime at the ANATOMIX beamline in February this year. The related analysis pipeline is presented in the current volume [23]. The incremental layers are seasonally deposited similarly to the well-known layers in a tree trunk. Thus, a pair of layers, consisting of dark and bright structures, represents one calendar year [24]. Resulting predictions of the season of death based on these layers [25] indicates tooth cementum as a tissue highly valuable for anthropology [24] and forensics [26]. The layer thickness is influenced by a number of factors including hormonal changes in pregnancy and stress events such as pathologies as well as nutrition as examined profoundly in recent studies [25, 27]. Nonetheless, cervical acellular extrinsic fiber cementum provides the steadiest growth rate conserving layer thickness [20, 21, 24]. Unfortunately, counting of layers is error-prone and observer-dependent, leading most commonly to an underestimation of age, despite of high-resolution imaging methods [28, 29]. Further investigation is therefore desired and suggested in archeological samples with corresponding life history [24, 29]. For these unique ancient samples, tomographic imaging should be favored to conventional microscopy, the latter requiring physical slicing [2]. In this study, we show to what extent the incremental can be detected by means of laboratory-based tomography setups. It can be reasonably assumed that owing to the developments in detector and X-ray source technology for the advanced instrumentation, the incremental layers could come to light.

1.3 Zebrafish embryo – a versatile biomedical research model

The zebrafish is a well-established animal for *in vivo* biomedical research. This rather basic vertebrate model offers an outstanding balance between relevant physiology and accessibility regarding ethical context, rapid and effective life-cycle and husbandry, as well as an attractive similarity to the human genome [30]. Therefore, the zebrafish finds numerous applications including studies in pathological conditions such as kidney injury [31] and treatment such as transplantation [32], to name a few. High-resolution hard X-ray tomography was used to examine single organ-centered anatomy of the zebrafish heart [33], muscles [34], as well as nanoparticle distribution [35]. In a recent study, synchrotron radiation was applied in whole-organism histotomography, enabling extraction of cellular architectures [36]. This study promises a broader understanding of anatomy and corresponding physiology and pathophysiology. Previously, we showed that more than 50 % of anatomical features identified by synchrotron radiation-based micro computed tomography (SRµCT) can also be identified with standard laboratory-based tomography systems [37]. We can, therefore, expect that the cutting-edge laboratory-based systems provide images comparable to the tomography setups at synchrotron radiation facilities. Such a success implies the possibility to easily perform large experimental series of high-resolution imaging fundamental in the zebrafish-based research activities.

1.4 Nerves – clinical application of hard X-ray tomography-controlled tissue engineering

Nerves show slow self-healing and a reinnervation potential after damage up to minimum 12-month post-injury following a degenerative phase. Surgical treatment might be needed, especially in neuronal endplates involvement, i.e. neurorrhaphy or even grafting in case of potential tension by end-to-end suturing [38]. Still, more than one fourth of patients do not regain motoric function [39] without substantial improvement over the last two decades [38, 39]. Additionally, quantification of nerve damage, currently making use of histology, assists in understanding pathomechanisms, diagnostics and therapy of multiple sclerosis [40] and vasculitis including Wegener's polyangiitis [41]. Nerve imaging and further investigations of nerve regeneration have been proposed using microtomography for imaging down to the sub-cellular level [3, 42]. In contrast to histology, phase-contrast microtomography of myelinated nerves provided visualization and quantification of the microanatomy of nerves and may lead to profound physiological comprehension [43, 44]. We hypothesize that advanced laboratory instrumentation leads to substantial improvement in microanatomical feature visibility compared to the established laboratory-based tomography systems [3, 42, 45].

1.5 Assessment of user-friendliness

A satisfying experience with a purchased product strongly depends on subjective evaluation on usability rather than only objective criteria such as effectiveness and efficiency [46]. Assessment of software user-friendliness has thus been well-established since the 1980s by standard questionnaires including the System Usability Scale, abbreviated SUS [46]. Crucial criteria appraised by the analysis of comments on tested systems include easy handling and intuitive design [47].

Unintuitive systems run the risk of malfunction, leading to reduced overall performance of technology and may even be hazardous in a medical context [48]. Therefore, we included user-friendliness of advanced laboratory systems as a valid purchasing criterion for next-generation systems. We integrated four criteria to appraise novice user experience in cutting-edge setups: (i) intuitive interface, (ii) structural organization, (iii) efficiency and effectiveness and, finally, (iv) reliability. These areas were scored by a beginner-level user who participated in the test measurements.

2. MATERIAL AND METHODS

2.1 Sample preparation

2.1.1 Preparation of porcine nerve for tomographic imaging

After excision, the peripheral nerves were processed following a standard histology protocol for formalin fixation and paraffin embedding. Briefly, the nerves were straightened by firmly tugging both ends with surgical forceps, then fixed in histology-grade 4 % formalin over a period of 24 hours, and dehydrated in ascending ethanol solutions. Subsequently, nerves were transferred to xylene and then perfused in a liquid paraffin–polymer mixture (Leica Paraplast, USA).

When liquid paraffin perfusion was completed, the nerves were removed from the histological tissue processor, placed in a metal container and left for a period of 24 hours inside an oven at a temperature of 60 °C. This step is important in removing air bubbles trapped inside or around the specimen, that can potentially cause artifacts during the X-ray imaging and compromise automatic data analysis. Subsequently, the specimens were thoroughly washed under flowing liquid paraffin, to remove high-absorbing particles or debris on the sample surface that would affect imaging quality. Finally, the nerves were immersed in paraffin several times while holding from one edge, until a uniform cylindric specimen was formed and then cooled down to a temperature of 4 °C over a period of 15 minutes.

2.1.2 Preparation of three-day-old paraffin-embedded zebrafish embryos

Three-day-old zebrafish embryos were euthanized using tricaine methanesulfonate containing 0.612 mM trisamino-methane. Subsequently, the embryos were fixated in 4 % paraformaldehyde at room temperature before refrigerating the samples at a temperature of 4 °C for storage. These fixed embryos were dehydrated in a dilution series of ethanol from 25 % via 50 % and 70 % to above 99.5 % in time steps of 15 minutes. Then, the dehydrated zebrafish embryos were washed twice in xylene, > 98 %, Carl Roth, Switzerland, and subsequently transferred into liquid paraffin at a temperature of 68 °C (Leica paraplast bulk, USA). After cooling, metal punches with inner diameters of 2.8 or 3.6 mm were used to cut out the embedded specimens to obtain cylinders for the imaging tasks. For the synchrotron radiation-based experiments, the paraffin cylinders were further manually trimmed in order to remove excess paraffin.

2.1.3 Selection of archaeological human tooth

The selected premolar tooth from the maxilla of a woman who died at the age of 36 comes from the reference skeleton series Basel-Spitalfriedhof, which is archived at the Natural History Museum Basel, Switzerland.

The skeletons come from a cemetery of the former Basel City Hospital and were exhumed in 1988 and 1989. Based on historical sources, it was possible to identify the skeletons of former hospital patients, who died between 1845 and 1868. In addition, further information on social and geographical origin, information on the living and working situation, medical histories, *etc.* is available. This detailed historical information combined with corresponding skeletons from the 19th century is unique worldwide and allows, for example, the reconstruction of biographies taking into account biological and historical sources. Furthermore, these skeletons are used for method verification and development of future methods.

2.2 Data acquisition with SkyScan 2214

The samples were mounted on a thin carbon fiber stage for high-resolution nanoCT scanning in the system SkyScan 2214. The X-ray camera was set in the "near" position with a source-camera distance of 235 mm. The acceleration voltage was set to 40 kV for the imaging of the zebrafish embryo, 30 kV for the porcine nerve bundle and 70 kV for the imaging of the tooth cementum. A 0.5 mm-thin Al filter was only applied for the data acquisition of the human tooth. A LaB_6 type source filament was employed for all scans. The individual scans were limited to a duration of almost eleven hours. The spot size was about 0.5 µm for the zebrafish and tooth radiograph recording and about 1.5 µm for the nerve bundle recording. The scan pixel sizes were set to 275, 800 and 750 nm for zebrafish, nerve bundle and tooth, respectively. Total numbers of recorded projections were 3,001, 2,401 and 2,118 for zebrafish, nerve bundle and tooth, respectively. Scans were acquired over 360°. Frame averaging was employed. For the zebrafish and tooth imaging two images were averaged while for the

tooth four images were used. Active ring artefact suppression by random horizontal (compensated) camera movement was done. A post-scan correction was applied [49] to minimize thermal movement artefacts. Image reconstruction was performed by Feldkamp-type cone beam algorithm [50] using Bruker NRecon™ software with GPU acceleration, applying Gaussian smoothing, ring artefact and beam hardening correction. Phase retrieval was done for the acquired data [51].

2.3 Data acquisition with Exciscope

The three selected samples were imaged at KTH Royal Institute of Technology in Stockholm, Sweden. The setup is based on the MetalJet D2 X-ray source (Excillum AB, Kista, Sweden), the XSight Micron LC 1080 sCMOS X-ray detector (Rigaku Innovative Technologies Europe s.r.o., Czech Republic) and the URS100BCC rotation stage (Newport, CA, USA). Both acquisition control and image reconstruction were done using the Exciscope software (Exciscope AB, Kista, Sweden). The experimental setup had a source-object distance of 225 mm and a source-detector distance of 280 mm. The effective pixel size was set to 1.28 µm at the scintillator and 1.03 µm at the object due to the geometric magnification. Projections were acquired equiangularly over a full 360° rotation. The reconstruction included phase retrieval with Paganin's method [52] and tomographic reconstruction using the FDK method [50]. The scan parameters for the three samples are listed in Tables 1 to 3.

2.4 Data acquisition with Xradia 620 Versa

X-ray microscopy measurements were performed on a Zeiss Xradia 620 Versa system (Carl Zeiss X-ray Microscopy, Inc., Dublin, USA). Projections of the samples were recorded in a unique two-stage magnification process that included optical magnification. The following acquisition parameters were selected. For the human tooth we used an acceleration voltage of 80 kV, a beam current of 125 µA, a 4× objective, narrowing of the X-ray bandwidth by the LE4 filter, 710 nm effective pixel size, rotation angle-dependent exposure time ranging from 7 to 14 s, and 2,501 projections. The porcine nerve was imaged with an acceleration voltage of 60 kV, a beam current of 108 µA, a 4× objective, 709 nm effective pixel size, exposure time of 6.2 s, and 3,201 projections. For the zebrafish data recording, we employed an acceleration voltage of 50 kV, a beam current of 90 µA, a 20× objective, 325 nm effective pixel size, 8 s exposure time, and 4,801 projections. The tomography datasets were reconstructed with the ZEISS Scout-and-Scan Reconstructor software using the cone-beam method for the tooth and zebrafish data and the OptiRecon method for the nerve data.

2.5 Data acquisition at the TOMCAT beamline

Synchrotron radiation-based phase-contrast X-ray microtomography measurements of zebrafish were acquired at the TOMCAT beamline X02DA of the Swiss Light Source (SLS) [53]. The X-ray beam generated by the 2.9 T superbend magnet was monochromatized to 12.0 keV at a bandwidth of around 2 % using a Ru/C double multilayer monochromator. Projection images of the sample placed about 25 m from the source were converted to visible light by a 20 µm-thick $Lu_3Al_5O_{12}$:Ce scintillator (Crytur, Turnov, Czech Republic) positioned 12 mm downstream of the sample. The image on the scintillator was magnified 20-fold by a visible light microscope (Olympus UPLAPO 20× objective) and recorded by a pco.Edge 5.5 sCMOS camera (PCO, Germany) with a native pixel size of 6.5 µm, resulting in an effective pixel size of 0.325 µm. During the continuous 180-degree rotation of the sample (parallel beam geometry), 2,000 projections with 200 ms exposure time were recorded for the reconstruction, resulting in an angular step of 0.09° and a scan time of 400 s. Additionally, 30 dark-field and 50 white-field images were recorded for image correction. Propagation-based phase contrast projections were calculated from the flat- and darkfield-corrected radiographs using Paganin's algorithm with the parameters $\delta = 10^{-7}$ and $\beta = 2\ 10^{-9}$ [52]. The absorption- and phase-contrast reconstructions were then computed from the corrected and phase-filtered projections, respectively, with the gridrec reconstruction algorithm [54].

2.6 Data acquisition at the ANATOMIX beamline

The measurements at the ANATOMIX beamline of Synchrotron SOLEIL [55] were made with a filtered white beam at a gap of 5.5 mm of the U18 in-vacuum undulator source of the beamline. The beam was filtered with 20 µm-thick Au and 100 µm-thick Cu. The resulting beam has an estimated photon mean energy of about 33 keV. The detector consisted of a 20-µm-thick $Lu_3Al_5O_{12}$:Ce scintillator (Crytur, Turnov, Czech Republic) coupled to a sCMOS detector (Hamamatsu Orca Flash 4.0 V2) with 2048×2048 pixels by microscope optics (Mitutoyo 10× M PLAN APO, numerical aperture 0.28) with a magnification of ten, resulting in an effective pixel size of 0.65 µm. At an electron current of 450 mA in the SOLEIL storage ring, the exposure time for each of the 9,000 projections per height step taken over a range of 360° was 50 ms. The scan was taken in continuous "on-the-fly" mode. With the time required for the acquisition of flat and dark images and including dead time, the overall scan time for each height step was around 10 minutes. Before the absorption-contrast reconstruction, the projections were Gauss-filtered with $\sigma = 1.25$ pixel to increase the contrast-to-noise ratio [56].

2.7 Data acquisition with nanotom m and SkyScan 1275

The parameters for data acquisition of the three selected specimens, *i.e.* paraffin-embedded zebrafish embryo, paraffin-embedded porcine nerve, and human tooth cementum, using the established microtomography systems nanotom m and SkyScan 1275 are given in Tables 1 to 3.

Table 1. Scanning parameters used in zebrafish embryo microtomography.

	Nanotom m	SkyScan 1275	SkysScan 2214	Exciscope	Xradia 620 Versa	TOMCAT
Source-camera distance [mm]	600	286.0	237.5	280.0	12.6	25,012.0
Source-object distance [mm]	6.5	13.7	8.65	225.0	6.0	25,000.0
Effective voxel size [µm]	1.1	3.7	0.33	1.28	0.33	0.325
Acceleration voltage [kV]	60	15	40	40	50	(12 keV)
Beam current [µA]	310	156	116	1,400	90	
Number of radiographs	720	720	3,001	3,600	4,801	2,000
Rotation steps [deg]	0.5	0.5	0.12	0.1	0.07	0.09
Exposure time [s]	9	2.5	4.7	7	8	0.2
Scan time [h]	2.5	4	10.5	7.25	14	0.15

Table 2. Scanning parameters used in porcine nerve microtomography.

	SkyScan 1275	SkysScan 2214	Exciscope	Xradia 620 Versa	ANATOMIX
Source-camera distance [mm]	286.0	235.2	280.0	44.35	170,050.0
Source-object distance [mm]	30.2	10.8	225.0	9.35	170,000.0
Effective voxel size [µm]	8.5	0.8	1.28	0.71	0.65
Acceleration voltage [kV]	20	30	40	60	(33 keV mean)
Beam current [µA]	175	150	1,400	108	
Number of radiographs	720	2,401	3,600	3,201	9,000
Rotation steps [deg]	0.25	0.15	0.1	0.11	0.04
Exposure time [s]	0.65	1.1	10	6.2	0.05
Scan time [h]	2.3	6.0	10.25	7.5	0.17

2.8 Data registration

The registration pipeline consisted of several steps. First, we found an approximate position in the SRµCT datasets corresponding to the volume imaged in the laboratory scanner. The laboratory-based volume was then manually pre-aligned with this SRµCT image region via ITK-SNAP [57] (version 3.8.0). The images were then automatically registered with an affine or similarity transformation employing the open-source registration toolbox elastix (version 4.9) [58, 59]. In the case of the zebrafish embryo and tooth specimens, the foreground region was determined by semi-automatic segmentation via thresholding and morphological operations. Image registration parameters were tuned by checking the progression of the image similarity measure during registration and by visually inspecting alignment. The original laboratory-based µCT volumes were transformed to the space of the SRµCT volumes region using cubic B-Spline interpolation, as this preserved image intensities better than nearest neighbor and linear interpolation [60]. Registrations of the porcine nerve bundle, zebrafish embryo and tooth cementum images were performed independently by three of the authors (G.R., M.O., and C.T.). The registration parameters are listed in Table 4.

Table 3. Scanning parameters used in human tooth cementum microtomography.

	SkysScan 2214	Exciscope	Xradia 620 Versa	ANATOMIX
Source-camera distance [mm]	235.2	280.0	128.55	170,050.0
Source-object distance [mm]	10.1	225.0	13.55	170,000.0
Effective voxel size [µm]	0.75	1.28	0.71	0.65
Acceleration voltage [kV]	70	70	80	(33 keV mean)
Beam current [µA]	80	1,400	125	
Number of radiographs	2,118	3,600	2,501	9,000
Rotation steps [deg]	0.17	0.1	0.14	0.04
Exposure time [s]	7	12	7 to 14	0.05
Scan time [h]	11	12.25	8.5	0.17

Table 4. Main registration parameters for three anatomies.

	Pig nerve bundle	**Zebrafish embryo**	**Tooth cementum**
Transformation	Similarity	Affine	Affine
Image similarity measure	Advanced Mattes mutual information	Normalized correlation coefficient	Normalized correlation coefficient
Multi-resolution image pyramid with three levels	4×, 2×, 1×	16×, 8×, 4×	4×, 2×, 1×
Number of iterations	3,000	4,000	2,000 or 3,000
Number of samples	65,536	8,192	130,000 or 1,950,000

2.9 Identification of anatomical structures

Representative slices of the tomography datasets were compared in anatomy to atlas data. For the paraffin-embedded porcine nerve, the porcine sciatic nerve model was used [61] and for the paraffin-embedded zebrafish embryo, the images were compared to histological slices published in the Zebrafish Lifespan Atlas (http://bio-atlas.psu.edu) [62]. Qualitative comparison was done for the zebrafish dataset, because the same region is imaged in every dataset.

3. RESULTS

The image quality is initially evaluated by visual assessment, *i.e.* microanatomical description, with subsequent calculation of the spatial resolution (SR). The representative cross-sectional virtual histology slices acquired with synchrotron radiation sources showed a wealth in anatomical features and, therefore, served as gold standard. In Section 3.1, we present the comparison of the porcine nerve and the zebrafish larva with the results of the currently available inhouse systems nanotom m and SkyScan 1275. Sections 3.2 to 3.4 contain the results of the next-generation laboratory systems for the three selected specimens in comparison to the synchrotron radiation-based microtomography data of the same specimens.

3.1 Descriptive microanatomy of selected tomographic slices

The characteristic anatomy of the peripheral, unprocessed, paraffin-embedded nerve consisting of epi-, peri- and endoneurium as well as primary nerve fiber bundles surrounded by myelin sheaths, especially well recognized in the zoom-in (Figure 1, right, lower part), location given by the yellow dashed boxes, is verified by the ANATOMIX beamline data with true micrometer resolution excluding the vasa nervorum due to contrast poverty. Oppositely, the SkyScan 1275 output

in absorption contrast mode, see Figure 1 left, enables distinction of nourishing blood vessels yet myelin sheaths remain hardly visible verifying its insufficient spatial resolution with a lack of phase contrast for the smaller anatomical features.

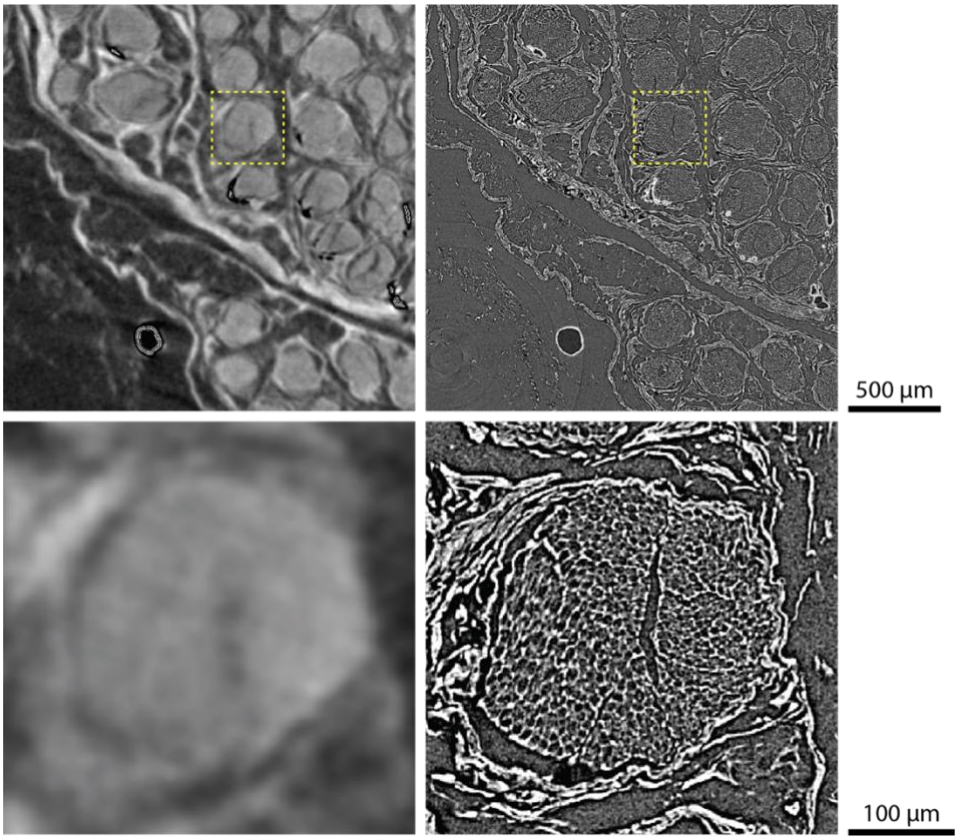

Figure 1. Corresponding cross-sectional slices of unprocessed, paraffin-embedded porcine nerves. Using 5 µm-wide pixels, the SkyScan 1275 (left) provides poorer spatial resolution in comparison to the ANATOMIX beamline (right) with 0.65 µm-wide pixels and propagation-based phase contrast, obtaining anatomical features down to the sub-cellular level. The zoom-ins in the lower part, location indicated by the yellow-colored dashed lines, show a selected nerve fiber bundle. It clearly demonstrates the gap between the established laboratory-based systems and the tomography setups at synchrotron radiation facilities.

Cross-sectional slices of the paraffin-embedded zebrafish embryo head are displayed in Figure 2. The data acquired at the TOMCAT beamline are phase-retrieved and demonstrate true single-cellular resolution. Especially, one can see mesencephalic and ophthalmic nuclei. Individual ocular cell layers that can be distinguished are the ganglion cells, inner plexiform, amacrine cells, photoreceptor layer and the retinal pigmented epithelium apart from the distinction between the bipolar and outer plexiform layers. Mesencephalic nuclei with high electron density are effortlessly separated from the surrounding. However, corresponding cartilage features around the pharynx remain low in contrast. The established laboratory-based systems SkyScan 1275 and nanotom m do not yield sufficiently high spatial resolution and contrast, respectively. Note that the nanotom m data hardly provides meaningful images of this low-absorbing specimen, since the aluminum layer on the detection unit suppresses photons with energies below 30 keV. Therefore, only the otoliths and the overall shape are visible to satisfying extent as shown in a recent study [35]. The SkyScan 1275 system allows the detection of photons with an energy down to 10 keV. Even two the ocular layers can be distinguished. The contrast between the denser nuclear mesencephalic region and its surrounding is satisfactory. The limited spatial resolution, however, prevents the true cellular resolution.

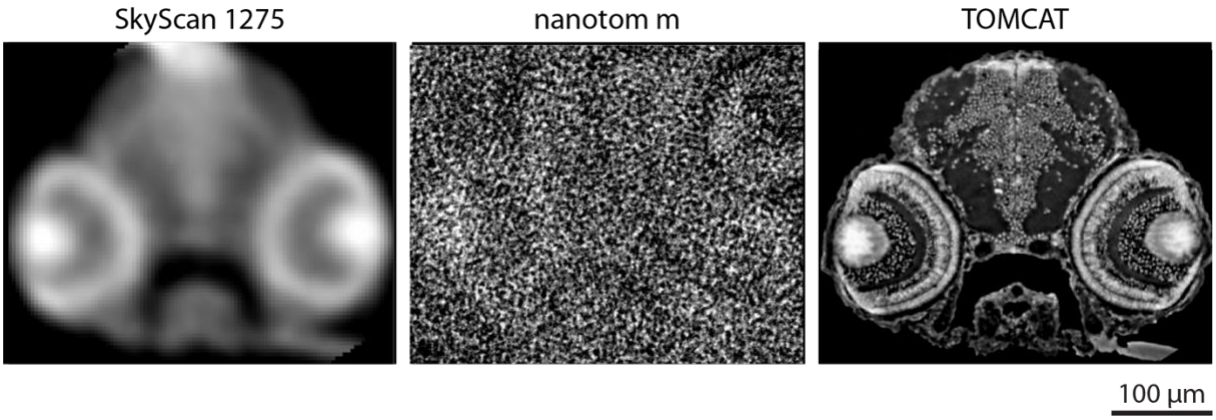

Figure 2. Corresponding virtual slices through the zebrafish embryo head by means of the established laboratory-based microtomography systems SkyScan 1275 and nanotom m in comparison with the data from the TOMCAT beamline, which can obviously serve as the gold standard in zebrafish embryo imaging.

3.2 Comparing the zebrafish embryo imaging of the next-generation laboratory-based scanners with the tomography available at the TOMCAT beamline

3.2.1 Performance of the SkyScan 2214

Figure 3 elucidates the leap in evolution from the established microtomography to the cutting-edge systems. Even the most affordable among the three systems, the SkyScan 2214, allows for the resolution of the individual cells within the zebrafish embryo head, especially well recognized in the images with higher magnification given on the right column. The similarity to the gold standard data is striking. The eye region with the ophthalmic cells, right images of Figure 3 were used for estimating the spatial resolution using the Fourier domain [63]. The instrument at the TOMCAT beamline yielded 1.3 µm, whereas the SkyScan 2214 data gave rise to 1.6 µm.

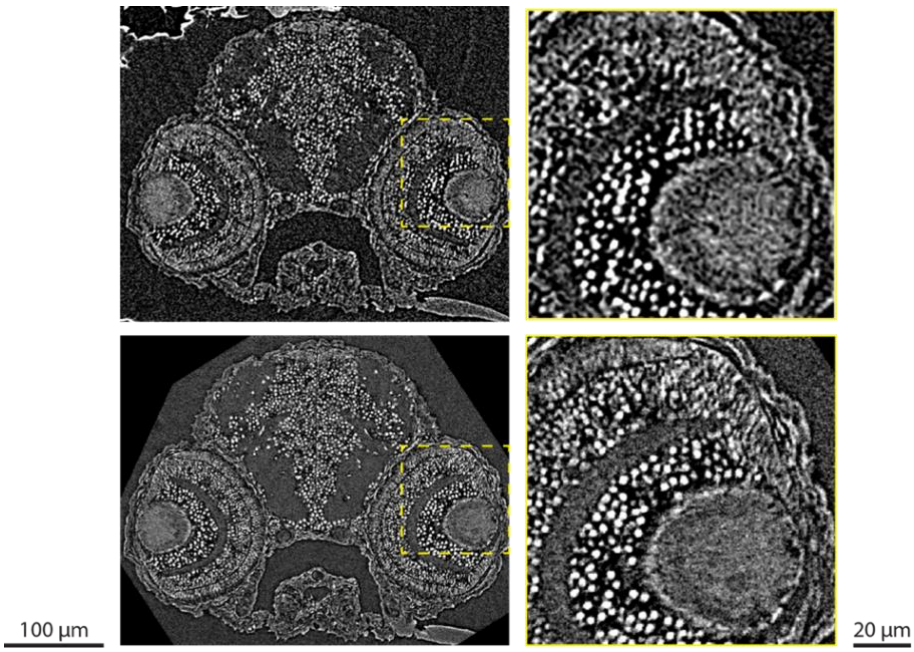

Figure 3. Corresponding virtual slices through the zebrafish embryo head by means of the cutting-edge, laboratory-based microtomography system SkyScan 2214 (top row) in comparison with the absorption-based tomography data from the TOMCAT beamline (lower row). The dashed yellow squares (left) indicate the position of the zoom-ins (right).

3.2.2 Performance of the Xradia 620 Versa

Figure 4 also shows the selected virtual slice through the zebrafish embryo recorded in the absorption contrast mode. The Xradia 620 Versa resembles even more the data from the TOMCAT beamline, most probably because of the same optical components of the detection system. Some edge enhancement is visible in both datasets, see for example the feature in the lower right corner of the left column. The eye region with the ophthalmic cells, right images of Figure 4, was used to estimate the spatial resolution [63]. The TOMCAT beamline data show a spatial resolution of 1.3 µm, whereas the Xradia 620 Versa data provided 1.6 µm.

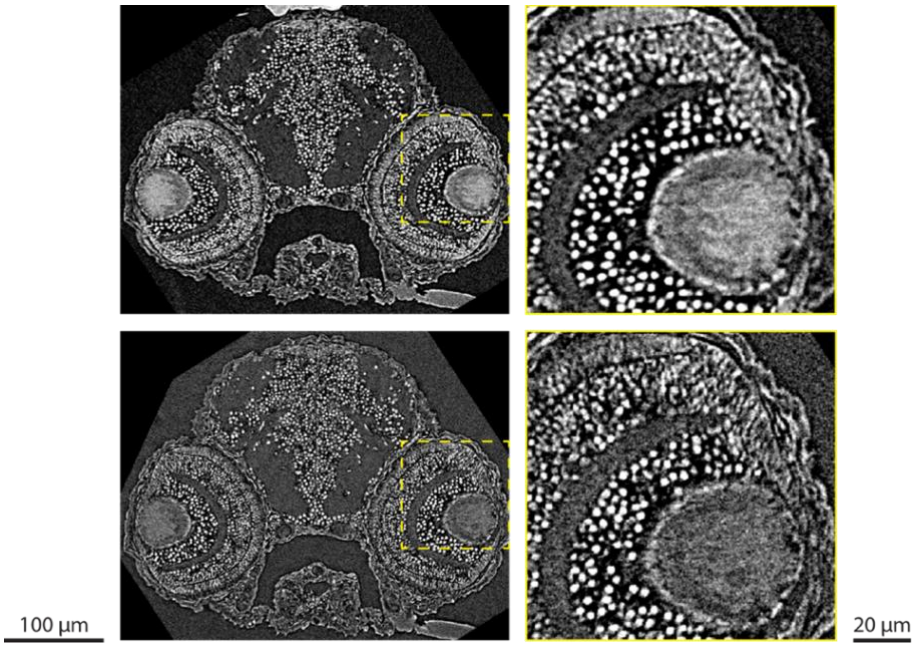

Figure 4. Corresponding cross-sectional slices through the zebrafish embryo head acquired at Xradia 620 Versa (above) and the TOMCAT beamline (below). The data shown is reconstructed without phase-retrieval. The dashed yellow squares (left) indicate the position of the zoom-ins (right).

3.2.3 Performance of the Exciscope

Figure 5 also shows the related virtual slices through the zebrafish embryo, but they have been prepared by including the phase retrieval with Paganin's method. Therefore, the TOMCAT beamline data exhibit modified contrast with respect to the images in Figures 2 to 4. In addition, the spatial resolution has been compromised. The cellular resolution was mostly preserved, although several anatomical features of the eye vanished owing to the noise level. This behavior is even more pronounced in the data of the Exciscope, most probably because of the less appropriate detector optics. The individual cells can hardly be recognized. Hence, the Exciscope system - in the configuration used - cannot resolve the cells within a paraffin-embedded zebrafish embryo. The eye region with the ophthalmic cells, right images of Figure 5, was also used for estimating the spatial resolution within the phase-retrieved datasets [63]. Here, the instrument from the TOMCAT beamline yielded 1.8 µm and the Exciscope 4.3 µm.

3.3 Comparing the imaging of annual layers in human tooth cementum applying the next-generation laboratory-based scanners and the microtomography of the ANATOMIX beamline

Applying the mosaic-style acquisition [64], the entire human tooth cementum was made visible by means of single-distance phase contrast tomography. This approach avoided the presence of artefacts known from local scans with true micrometer resolution when objects with centimeter diameters were studied. Thus, the local tomography data from the three selected next-generation, laboratory-based tomography systems could be registered to the large dataset from the ANATOMIX beamline. This approach was helpful since the local tomography at pre-defined positions could not be guaranteed. Therefore, Figures 6 to 8 and Videos 1 to 3, see below, do not cover the same regions of the human tooth, but have been always registered to the same ANATOMIX dataset. Consequently, the comparability of the tomography data from the cutting-edge instrumentation is definitely given.

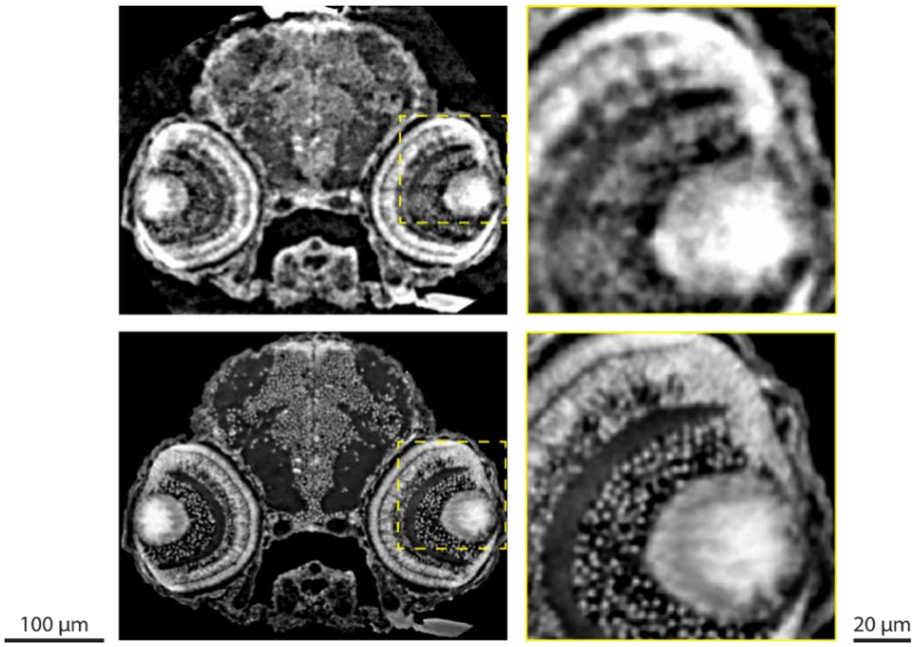

Figure 5. Corresponding virtual slices through the head of the zebrafish embryo acquired at Exciscope (above) and TOMCAT beamline (below). The dataset shown is reconstructed with phase-retrieval. The dashed yellow squares (left) indicate the position of the zoom-ins (right).

3.3.1 Performance of the Exciscope tomography system

Figure 6 displays a part of the human tooth with the following anatomical features: In the upper part, one finds the dentin with a crack of characteristic morphology. In the middle, the tooth cementum with the annual layers could be found. The lower part in black represents the surrounding air. Whereas the annual layers are easily recognized within the data from the ANATOMIX beamline, indicated by the yellow-colored arrow, the Exciscope instrumentation in the configuration used could not resolve these 2 to 3 µm-thin anatomical features. An objective with higher resolution might master this deficiency. These findings are further elucidated by Video 1. Note, Video 1 explicitly shows that the thin lines, usually termed incremental lines, are actual three-dimensional layers, given by the continuity of the visible lines scrolling through the 160 slices of the synchrotron radiation-based dataset.

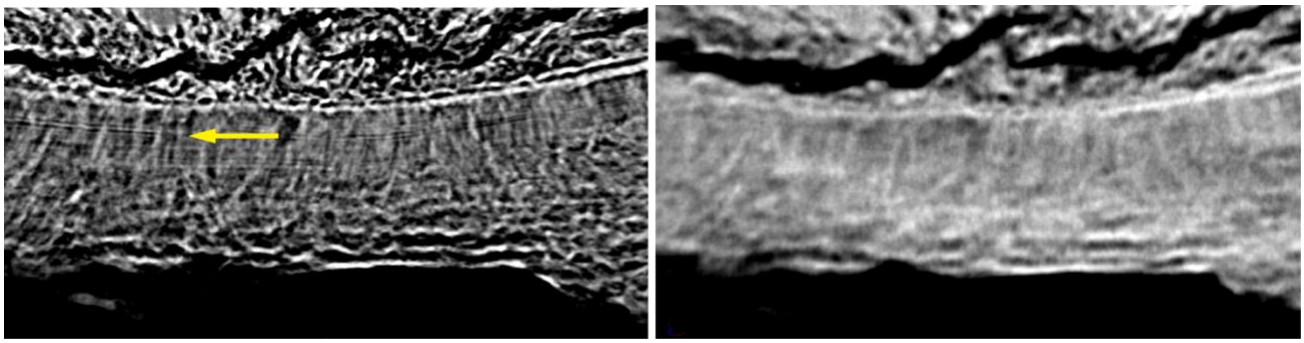

Figure 6. Selected virtual slices of tooth cementum acquired at ANATOMIX beamline, left image, and Exciscope, right image. The registered data are represented in a special three-dimensional fashion: 100 slices were rendered using the "Sum along ray" tool from VGStudio MAX to improve the visibility of the incremental layers, see yellow arrow.

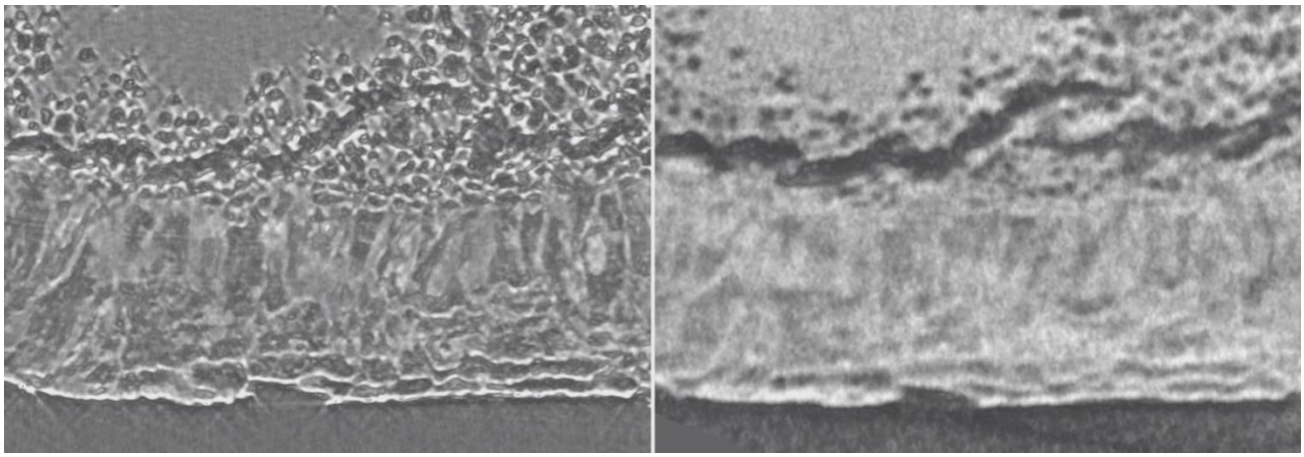

Video 1. Scroll-through 160 cross-sectional virtual histology slices, prepared by the software VGStudio MAX, of the human tooth obtained at the ANATOMIX beamline (left) and corresponding local scan by means of the Exciscope system with an *a priori* phase-retrieval (right). The annual layers are invisible in the latter dataset. The length of each box equals to about 0.6 mm. http://dx.doi.org/10.1117/12.2597926.1

3.3.2 Performance of the SkyScan 2214

The part of the human tooth shown in Figure 7 is a better choice than the one in Figure 6, because many annual layers can be traced from left to right within the data from the ANATOMIX beamline. As found previously [2], the 2 to 3 µm-thin annual layers are much clearer in the low-absorbing parts of the tooth cementum. The SkyScan 2214 setup, however, only shows contrast between the lower and higher X-ray-absorbing regions in the tooth cementum, but the annual layers remain invisible. This observation is also supported by Video 2, when scrolling through the 160 selected virtual slices obtained from the datasets of the two tomography systems.

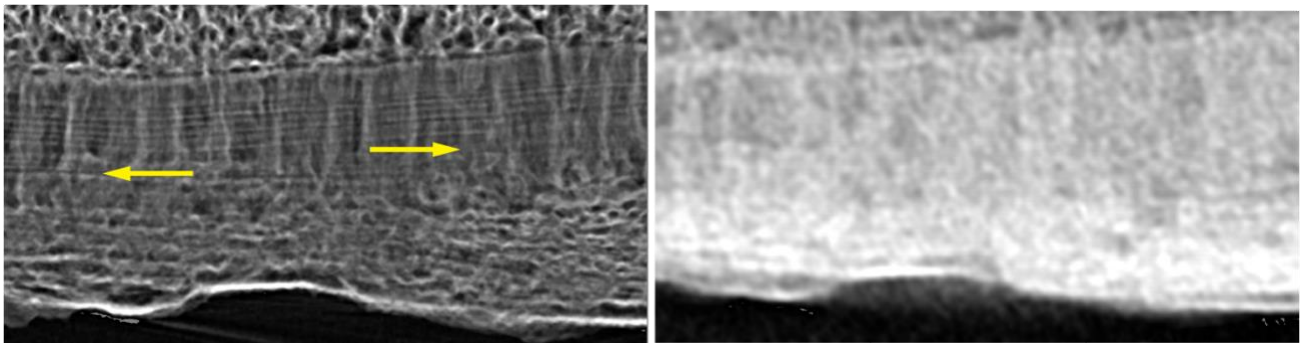

Figure 7. Selected virtual slices of tooth cementum acquired at ANATOMIX beamline, left image, and SkyScan 2214, right image. The registered data are represented in a special three-dimensional fashion: 100 slices were rendered using the “Sum along ray” tool from VGStudio MAX to improve the visibility of the incremental layers, see yellow arrow.

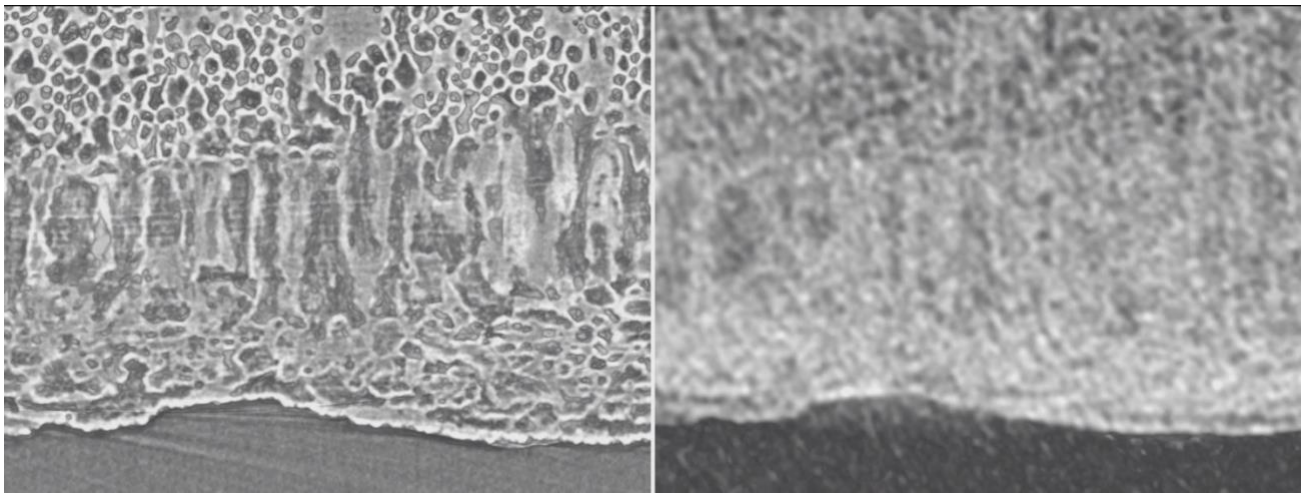

Video 2. Scroll-through 160 cross-sectional virtual histology slices, prepared by the software VGStudio MAX, of the human tooth obtained at the ANATOMIX beamline (left) and corresponding local scan by means of SkyScan 2214 without phase-retrieval (right). The annual layers are invisible in the latter dataset. The length of each box equals to about 0.6 mm. http://dx.doi.org/10.1117/12.2597926.2

3.3.3 Performance of the Xradia 620 Versa

Figure 8 and Video 3 demonstrate that the annual layers can also be made visible with a laboratory-based system. Although the Xradia 620 Versa does not reach the resolution of the synchrotron radiation-based setup, this result is promising and could even be further improved by substantially increasing the acquisition time. Note, the manufacturers had only 36 hours to image the three selected samples and the flux from the laboratory sources is orders of magnitude less than that of the synchrotron radiation facilities.

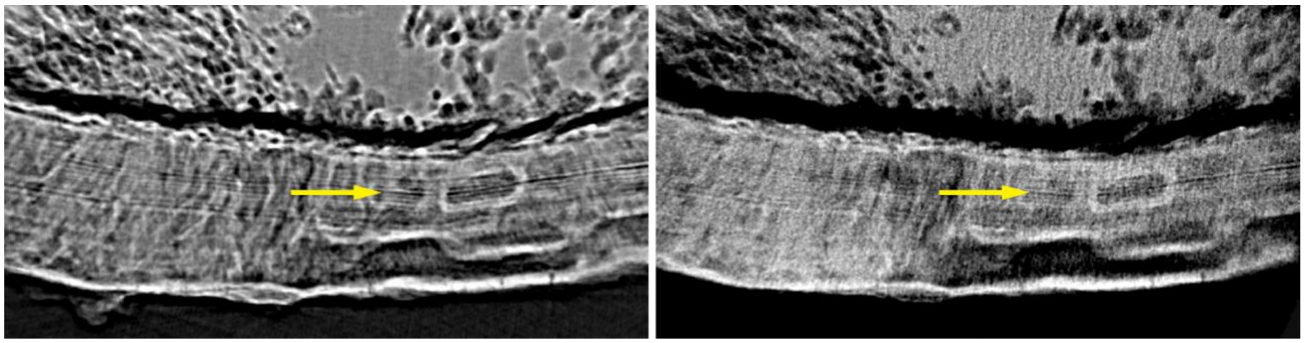

Figure 8. Selected virtual slices of tooth cementum acquired at ANATOMIX beamline, left image, and Xradia 620 Versa, right image. The registered data are represented in a special three-dimensional fashion: 100 slices were rendered using the "Sum along ray" tool from VGStudio MAX to improve the visibility of the incremental layers, see yellow arrow. The annual layers are not only visible in the data acquired at the synchrotron radiation facility but also in the dataset gathered at the cutting-edge laboratory-based system.

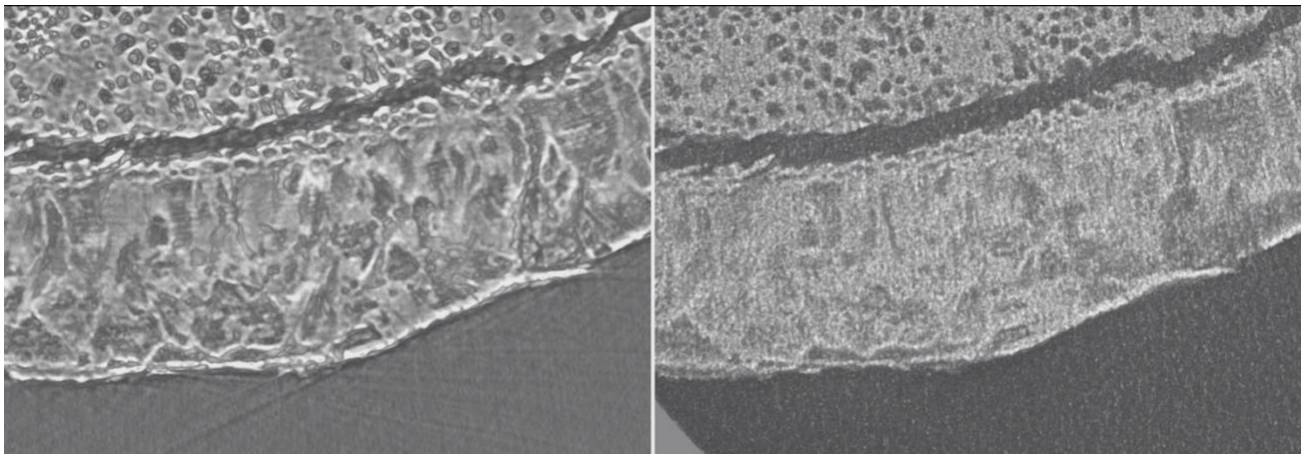

Video 3. Scroll-through 160 cross-sectional virtual histology slices, prepared by the software VGStudio MAX, of the human tooth obtained at the ANATOMIX beamline (left) and corresponding local scan by means of Xradia 620 Versa without phase-retrieval (right). The annual layers detectable in both datasets. The length of each box equals to about 0.6 mm. http://dx.doi.org/doi.number.goes.here

3.4 Comparing the three-dimensional imaging of the spiral organization in a paraffin-embedded porcine nerve applying the next-generation laboratory-based scanners and the microtomography of the ANATOMIX beamline

Similar to the tooth imaging, the paraffin-embedded nerve with a diameter of 6 mm does not fit into the field-of-view of the microtomography setups. Therefore, the mosaic-style acquisition [64] was also applied for the porcine nerve imaging at the ANATOMIX beamline. Again, the local tomograms from the cutting-edge laboratory-based instruments were registered to the data acquired at the ANATOMIX beamline. Videos 4 to 6 show a part of the registered data comparing the gold standard from the ANATOMIX beamline with the selected cutting-edge laboratory-based systems Xradia 620 Versa, SkyScan 2214, and Exciscope, respectively. One clearly recognizes a spiral structure of the nerve fiber bundles. This structure can be approximated by right-handed or left-handed helices with a pitch of about 830 µm.

3.4.1 Performance of the Xradia 620 Versa

Video 4 clearly demonstrates the substantial improvement of the Xradia 620 Versa imaging with respect to the SkyScan 1275 system, cp. Figure 1. Nevertheless, the myelin sheaths could only be hardly resolved. Regardless, one can detect the spiral structure of the nerve fiber bundles.

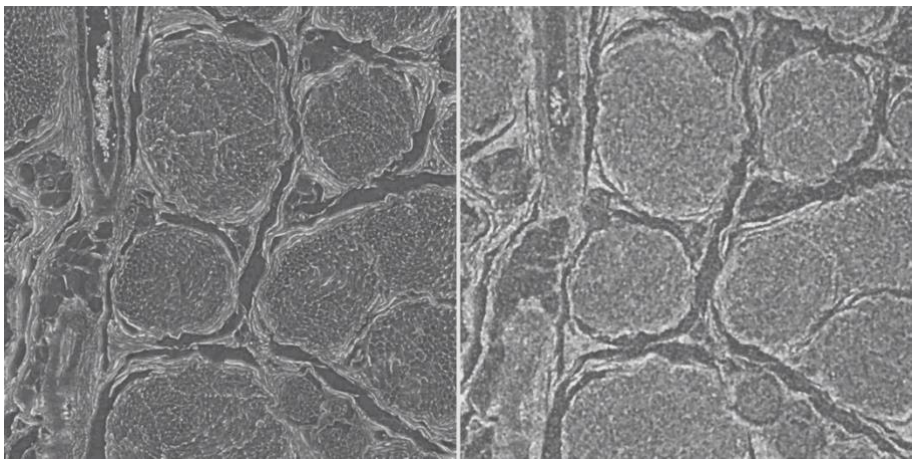

Video 4. Scroll-through 160 cross-sectional virtual histology slices, prepared by the software VGStudio MAX, of the porcine nerve obtained at the ANATOMIX beamline (left) and registered local tomography data of Xradia 620 Versa (right), both without phase-retrieval. The spiral structure of the primary nerve fiber bundles is recognized via a rotation during the scrolling. One image corresponds to an area of $(0.78\ \mathrm{mm})^2$. http://dx.doi.org/10.1117/12.2597926.4

3.4.2 Performance of the SkyScan 2214

The myelin sheaths are even slightly better visible in the tomography data of the SkyScan 2214 instrument, as demonstrated by Video 5. It is hardly surprising that the data of the laboratory-based system show much more noise that the ones from the synchrotron radiation facility, as it is easily explained by the photon statistics.

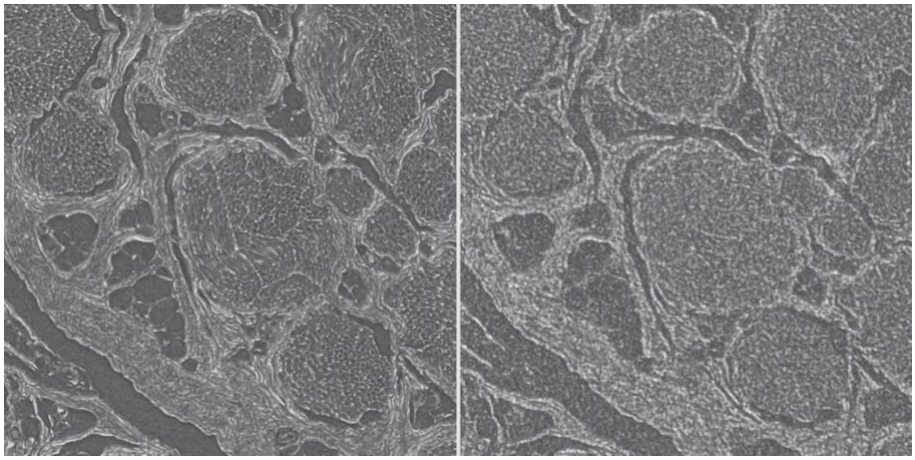

Video 5. Scroll-through 160 cross-sectional virtual histology slices, prepared by the software VGStudio MAX, of the porcine nerve obtained at the ANATOMIX beamline (left) and registered local tomography data of the SkyScan 2214 (right), both without phase-retrieval. The spiral structure of the primary nerve fiber bundles is clearly recognized via a rotation during the scrolling. One image corresponds to an area of $(0.78\ \mathrm{mm})^2$. http://dx.doi.org/10.1117/12.2597926.5

3.4.3 Performance of the Exciscope tomography system equipped with a liquid metal source

Because the Exciscope is equipped with a liquid metal source, the photon flux is much higher than for the other two laboratory-based tomography devices. With the better photon statistics, the density resolution is superior, as seen by the well-preserved myelin sheaths in Video 6. This phenomenon is even enhanced by the implemented phase retrieval, see Video 6. Consequently, the spiral structure is clearer visible. Note, the presence of right- and left-handed spirals.

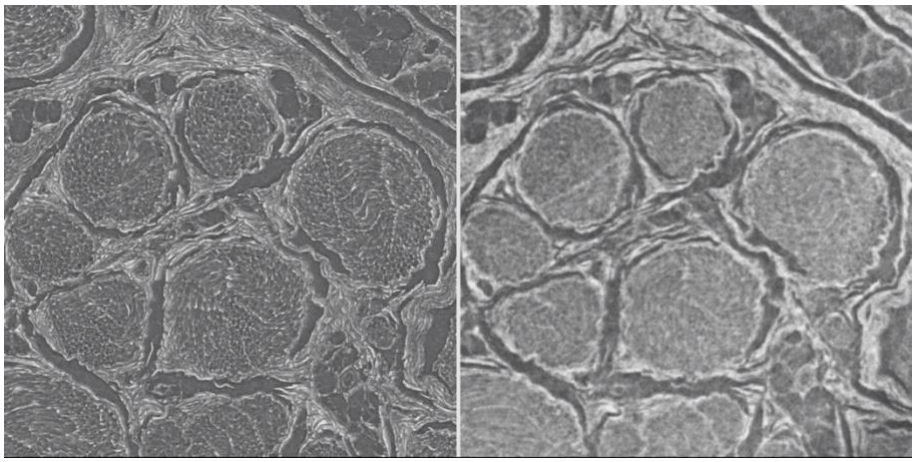

Video 6. Scroll-through 160 cross-sectional virtual histology slices, prepared by the software VGStudio MAX, of the porcine nerve obtained at the ANATOMIX beamline (left) and registered local tomography data of the Exciscope (right) with phase-retrieval. The spiral structure of the primary nerve fiber bundles is well recognized via a rotation during the scrolling. One image corresponds to an area of $(0.78\ \mathrm{mm})^2$. http://dx.doi.org/10.1117/12.2597926.6

4. DISCUSSION

4.1 Limitations

The comparative study of the next-generation tomography systems for virtual histology has several drawbacks, as already pointed out by the manufacturers during the data acquisition. First, the 36 hour limit for the imaging of the three medically relevant specimens was considered as too short. Longer periods of scanning time would most probably yield to improved results. This argumentation is reasonable, especially because the reference images from the synchrotron radiation facilities had been acquired with much higher photon flux. The present study did not consider the unequal numbers of photons used for the individual tomograms.

The measurements by means of the SkyScan 2214 system in March 2021 have not reached the expected data quality. Therefore, the measurements were repeated in July 2021, which might have resulted in a bias for direct comparison.

The Exciscope system is rather a prototype than a tuned microtomography machine (status March 2021). Therefore, the optics only allowed for data acquisition with an effective pixel size of 1.3 µm. Just exchanging a standard optical element will allow for pixel sizes of 0.65 µm.

The Xradia 620 Versa setup could only provide reconstructions based on absorption contrast (status March 2021). The manufacturer, however, stated that a feature for image enhancement using phase contrast will be available soon.

This lack of phase-retrieval for the Xradia 620 Versa system and the limited pixel size of the Exciscope system made a direct comparison of the contrast-to-noise ratio (CNR) impossible. Together with the spatial resolution, CNR is an essential metric to assess the image quality of the acquired tomograms [56].

The spatial resolution depends not only on the pixel size employed, but also on many other parameters such as the mechanical stability of the entire system and the design of the detection unit. The spatial resolution we have calculated should be treated with care, because the analysis of the power spectrum of reconstructions used here [63, 65] is challenging and less straightforward than e.g. measurement of test patterns. Nonetheless, the quantities derived with the model of Mizutani *et al.* [63] perfectly related to the visual inspection.

4.2 Summary of the system comparison

The SkyScan 2214 setup consists of up to three cameras, which can be easily exchanged by the user. Depending on the desired spatial resolution and flux, W or LaB_6 cathodes can be implemented. The set-up with the selected parameters is well suited to image tiny specimens such as the paraffin-embedded zebrafish embryo with a diameter of less than 1 mm down to true cellular resolution, cp. Figure 3. The myelin sheaths in a paraffin-embedded porcine nerve were partially distinguishable, cp. Video 5. The annual layers of the human tooth cementum were impossible to be detected (Figure 7).

The tomography setup from Exciscope takes advantage of a liquid metal source with substantially increased brightness [66] at the expense of spot size (see Tables 1 to 3). During the comparative study, the prototype was only equipped with an optics for 1.3 µm effective pixel size. This setup led to a reasonable visibility of myelin sheaths, cp. Video 6 and excellent contrast in the zebrafish embryo without achieving full cellular resolution, cp. Figure 5. The annual layers in the tooth cementum could not be made visible, cp. Figure 6, in March 2021. Nevertheless, the authors are confident that the further improvements of the prototype will lead to a spatial resolution well below 2 µm.

The Xradia 620 Versa uses sophisticated optics, which provides excellent tomography data, even with the standard X-ray source. The image quality is impressive. Most impressive is the identification of the annual layers in tooth cementum, cp. Figure 8.

Despite the leap in evolution from the established microtomography to the cutting-edge systems, one can find some gap to the synchrotron radiation-based setups. These experimental setups enabled imaging the entire nerve and tooth with laterally extended field-of-view thanks to the parallel beam geometry and a at least 50 times faster data acquisition.

4.3 Zebrafish larva – full-specimen imaging in pre-medical studies

The capacity for true micrometer resolution imaging with the selected laboratory-based systems was assessed by means of the zebrafish larva. A wealth of anatomical features could be detected with the advanced instrumentation. The Xradia 620 Versa showed the highest resolution, *i.e.* down to single nuclei, however, the contrast of the provided images could be further improved with phase-retrieval. The SkyScan 2214 showed a likewise high-quality dataset with a slight increase in noise. Clear distinction of cells was almost impossible with Exciscope that nonetheless showed satisfactory layer

separation within the eye. Note that this was achieved in unstained samples whereas previously, staining was widely used with laboratory instrumentation [33]. A detailed comparison of the three X-ray microscopes was impossible, as at the time of our measurement, *i.e.* March 2021, phase-retrieval was inaccessible in Europe for the Xradia 620 Versa, SkyScan 2214 data measurements had to be repeated and the Exciscope prototype only provided detector optics with an effective pixel size of 1.3 µm. By visual inspection, however, the advances in table-top µCT systems in comparison to the established systems in our lab is evident, leading to an image quality close to that of SRµCT.

Recent studies of zebrafish, for example the complete histological phenotyping [36] and the determination of nanoparticle distribution [35], have relied on SRµCT. Based on the present results with the cutting-edge µCT systems, future studies of the zebrafish embryo in a laboratory setting are planned. Moreover, with the attractive homology to humans as underlined by exemplary drug target conservation [67], further investigations on pharmacological and phenomics studies with high-resolution imaging of organs and the whole zebrafish will be led by cellular resolution in an accessible setup for fast-feedback and follow-up imaging. This volumetric imaging provides three-dimensional context in contrast to conventional histology serving as alternative for pharmacological studies. Future studies of the zebrafish include pharmacological kidney failure as structure and pathomechanism of renal epithelial injury [31].

4.4 Human tooth cementum – requirement for non-destructive imaging technique in unique samples

Until now, incremental layers may only be imaged to satisfying extent at synchrotron radiation facilities [29] or by means of conventional optical microscopy of thin sections [24, 26, 28]. A laboratory-based µCT was suggested by G. Mani-Caplazi [2] based on physically sliced samples and a close source-sample position. Here, we showed that the advanced laboratory instrumentation yields great potential for facilitating high-resolution imaging of incremental layers in a non-destructive manner. Barely identifiable lines in the tooth cementum obtained with the Xradia 620 Versa were enhanced by 3D rendering of 100 slices. High-resolution three-dimensional imaging of the human tooth cementum as in the SRµCT or µCT provides sufficient anatomical context to show that the thin lines actually correspond to curved three-dimensional layers [68] which we showed in the scroll-through Videos 4 to 6 where those lines were continuous.

Our findings show great potential for laboratory sources in ongoing research of the tooth cementum annulation (TCA). This phenomenon has been studied in humans for around four decades [24]. However, there is as of yet neither a coherent explanation nor a standard protocol for tooth selection, preparation and layer counting, yet many advances have been made [24, 26]. Laboratory-based µCT may benefit region selection applied *a priori* to SRµCT [2] or conventional microscopy where samples are cut irreversibly in about 100 µm-thin slices [28]. Further, the promising results of the Xradia 620 Versa indicate that laboratory-based µCT alone could be used to quantify these layers, for example in large-scale studies of archeological samples with recorded history to standardize age estimation or examine of influencing factors for the layer growth. This approach might be extended to animal studies.

4.5 Nerve – clinical application

High-density resolution and sub-micrometer spatial resolution are required to quantify changes in axonal bundles and myelin sheaths as the result of nerve injury and regeneration. We showed that the cutting-edge tomography systems SkyScan 2214, Xradia 620 Versa and Exciscope yield enough spatial and density resolution enabling visibility of several myelin sheaths and axonal bundles. Therefore, X-ray virtual histology combined with bioengineering could facilitate protocols for stepwise de- and re-cellularization including follow-up laboratory imaging for fast feedback control. Already, laboratory-based µCT with or without combination of conventional histology can assist in studies of nerve regeneration including grafting [45, 69]. Furthermore, µCT could support the urgent diagnostic need of Wegener's polyangiitis [70] whose gold standard is biopsy [41]. Moreover, µCT allows for further investigation of pathomechanisms of this vasculitis and other neurovascular diseases by computational extraction of neurovascular networks [71] or support three-dimensional prospective mapping of neuron connectivity in order to understanding anatomical context [72]. Based on the image quality demonstrated here, we expect further integration of advanced µCT into the study of nerve disease, injury, and regeneration.

In Videos 4 to 6, the spiral shape of nerve bundles is observed as one scrolls through the reconstructed slices. This behavior has been described previously as a "shevron pattern" in longitudinal histotomographical nerve slices [43, 44], however, the function of this pattern warrants further investigation. An explanation could be a gain of stability, analogous to (steel) wire ropes [73].

4.6 User-friendliness

The main author, a Master student in medicine, together with the second author, an experienced physicist and expert in the field, observed the 36-hour measurements at the three manufacturers of the cutting-edge, laboratory-based

microtomography systems. During the setup of the experiments, the software of the X-ray microscopes was explained in detail. The user-friendliness of the software was compared on the basis of (i) intuitive interface, (ii) structural organization, (iii) efficiency and effectiveness, and (iv) reliability.

Overall, the novice performance was best supported by the Xradia 620 Versa software. This interface allowed for a rather simple and intuitive measurement setup. Proceeding through the well-structured software required user input, which was assisted by the compact two-page manual. A live camera showed the sample position within the instrument. Time saving and precise sample centering was based on double-clicking on radiographs at 0° and 90° rotation angles. A single click allowed for repositioning of the sample along the *x*-, *y*- and *z*-axis as well as the source and detector along a single axis. Fragile samples were protected from collisions by automatic measurement of the sample diameter. Filter and source settings could be comfortably modified via software. A table in the short two-page overview assisted in choosing the best suitable filter. Rapid pre-scanning enabled scouting. Subsequent fine-tune centering was performed automatically after manual center identification in the pre-scan data. In addition, "recipes" could be created to facilitate a session for scanning multiple samples. The estimated scanning time was met.

Bruker's software of the SkyScan 2214 was likewise pleasant. The interface, however, was less self-explanatory. It consisted of one screen combining visualization of the sample using a camera, an immense live-view X-ray window and the necessary settings. This approach was advantageous for experienced users, yet a novice might miss essential adjustments due to absence of guidance through the preparation steps. Additional settings were hidden in the "Options" panel. The sample could be rotated by 360° and relocated in *x*-, *y*- and *z*-direction, automatically. Translation in *x*- and *y*-dimensions was simplified by drag-and-drop. Additionally, the detector could be mechanically moved in one dimension. Automatic sample protection was unavailable. Source and filter could be chosen comfortably via software. The selection of these settings, however, was not guided and linked to the user's prior experience with measurements. Similar to the Xradia 620 Versa, rapid pre-scanning allowed for scouting. Fine-tune centering was performed manually. The estimated scanning time was generally reliable, although it once underestimated the required scan time.

The user-friendliness of Exciscope could not be assessed. The prototype was missing a user-interface in March 2021 when the measurements took place. The prototype required numerous modifications that precluded operation by a novice user. The reliability of the estimated scan time was satisfactory.

In summary, the software of the Xradia 620 Versa persuaded in the defined criteria. Bruker's software of the SkyScan 2214 offered an almost similarly satisfactory interface with less simplicity. No user-friendliness could be assessed for the prototype of Exciscope.

4.7 Laboratory-based phase tomography

The present study belongs to the few comparative experimental approaches on microtomography [13, 14, 16] and should support the purchase of the next-generation, laboratory-based systems, especially for the field of medicine. Now, the time is ripe to combine absorption and phase tomography in a single laboratory-based device and reach an isotropic spatial resolution close to 1 µm. The gap between the tomography setups at the synchrotron radiation facilities and the established laboratory-based microtomography systems is becoming more and more narrow.

The volumetric evaluation of tissues of human and animal origin is currently mainly done by serial sectioning, staining and microscopic imaging of the individual slices. This approach has drawbacks, such as the restricted spatial resolution perpendicular to the slices and the numerous preparation artefacts. High-resolution hard X-ray tomography can complement histology. Prior to sectioning, the stained and unstained tissues can be made visible in absorption and phase contrast modes to extract local densities. Histotomography similarly facilitates decision-making in cutting location and angle of a probe for further histological examination [74]. Similarly, laboratory-based phase tomography can support choosing a region of interest prior to valuable beamtimes at tomography stations.

The zebrafish embryo is an appropriate example to demonstrate the complementary information from absorption and phase contrast modes, see Figures 3 to 5. The combination of the three-dimensional data using a bivariant histogram can allow for dedicated segmentation tasks [75].

5. CONCLUSION

Thanks to advances in instrumentation over the last decade, propagation-based phase-contrast microtomography is no longer reserved for synchrotron radiation facilities. Laboratory X-ray microscopes can provide satisfying (sub-)cellular

resolution to visualize anatomical features with true micrometer resolution. The compared scanners will be further complemented, but can already provide high-quality datasets of medically relevant, hard and soft tissue specimens. These laboratory systems do not only support beamtime planning by *a priori* non-destructive isotropic overview scans, but also be used in stand-alone imaging. Such imaging can be applied for the analysis of tooth cementum annulation in mammals, pre-clinical trials to quantify pathological mechanisms through the versatile zebrafish model, as well as pre-clinical and clinical trials towards regeneration and grafting of nerves.

ACKNOWLEDGEMENTS

We are grateful to the Swiss National Science Foundation for the financial support within the project Micro- and Nanotomography (grant 133802). We acknowledge the Paul Scherrer Institut, Villigen, Switzerland for provision of synchrotron radiation beamtime at the TOMCAT beamline X02DA of the Swiss Light Source and the Synchrotron SOLEIL for provision of synchrotron radiation beamtime at the ANATOMIX beamline within the frame of proposal 20200712. ANATOMIX is an Equipment of Excellence (EQUIPEX) funded by the *Investments for the Future* program of the French National Research Agency (ANR), project NanoimagesX, grant no. ANR-11-EQPX-0031. We thank Hans Hertz, KTH Stockholm Sweden, for his kind introduction and support at the Exciscope facility (Stockholm, Sweden).

REFERENCES

[1] Schulz, G., Deyhle, H., and Müller, B., [Imaging the human body: Micro-and nanostructure of human tissues], Springer, 69-94 (2012).

[2] Mani-Caplazi, G., Schulz, G., Deyhle, H., Hotz, G., Vach, W., Wittwer-Backofen, U., and Müller, B., "Imaging of the human tooth cementum ultrastructure of archeological teeth, using hard X-ray microtomography to determine age-at-death and stress periods," Proc. SPIE 10391, 103911C (2017).

[3] Bikis, C., Thalmann, P., Degrugillier, L., Schulz, G., Müller, B., Kalbermatten, D. F., Madduri, S., and Hieber, S. E., "Three-dimensional and non-destructive characterization of nerves inside conduits using laboratory-based micro computed tomography," Journal of Neuroscience Methods 294, 59-66 (2018).

[4] Osterwalder, M., Bolten, J. S., Rodgers, G., Schulz, G., Tanner, C., Cörek, E., Huwyler, J., and Müller, B., "Three-dimensional X-ray microscopy of zebrafish larvae," Proc. SPIE 11586, 115860J (2021).

[5] Töpperwien, M., van der Meer, F., Stadelmann, C., and Salditt, T., "Three-dimensional virtual histology of human cerebellum by X-ray phase-contrast tomography," Proceedings of the National Academy of Sciences 115(27), 6940-6945 (2018).

[6] Momose, A., "Recent advances in X-ray phase imaging," Japanese Journal of Applied Physics 44(9R), 6355 (2005).

[7] Paganin, D., [Coherent X-ray optics], Oxford University Press on Demand, (2006).

[8] Bravin, A., Coan, P., and Suortti, P., "X-ray phase-contrast imaging: from pre-clinical applications towards clinics," Physics in Medicine & Biology 58(1), R1 (2012).

[9] Endrizzi, M., "X-ray phase-contrast imaging," Nuclear Instruments and Methods in Physics Research Section A: Accelerators, Spectrometers, Detectors and Associated Equipment 878, 88-98 (2018).

[10] Khimchenko, A., Schulz, G., Thalmann, P., and Müller, B., "Implementation of a double-grating interferometer for phase-contrast computed tomography in a conventional system nanotom® m," APL Bioengineering 2(1), 016106 (2018).

[11] Lang, S., Zanette, I., Dominietto, M., Langer, M., Rack, A., Schulz, G., Le Duc, G., David, C., Mohr, J., Pfeiffer, F., Müller, B., and Weitkamp, T., "Experimental comparison of grating-and propagation-based hard X-ray phase tomography of soft tissue," Journal of Applied Physics 116(15), 154903 (2014).

[12] Zanette, I., Lang, S., Rack, A., Dominietto, M., Langer, M., Pfeiffer, F., Weitkamp, T., and Müller, B., "Holotomography versus X-ray grating interferometry: A comparative study," Applied Physics Letters 103(24), 244105 (2013).

[13] Töpperwien, M., van der Meer, F., Stadelmann, C., and Salditt, T., "Correlative x-ray phase-contrast tomography and histology of human brain tissue affected by Alzheimer's disease," NeuroImage 210, 116523 (2020).

[14] Khimchenko, A., Deyhle, H., Schulz, G., Schweighauser, G., Hench, J., Chicherova, N., Bikis, C., Hieber, S. E., and Müller, B., "Extending two-dimensional histology into the third dimension through conventional micro computed tomography," NeuroImage 139, 26-36 (2016).

[15] Khimchenko, A., Bikis, C., Pacureanu, A., Hieber, S. E., Thalmann, P., Deyhle, H., Schweighauser, G., Hench, J., Frank, S., Müller-Gerbl, M., Schulz, G., Cloetens, P., and Müller, B., "Hard X-Ray nanoholotomography: Large-Scale, label-Free, 3D neuroimaging beyond optical limit," Advanced Science 5(6), 1700694 (2018).

[16] Drews, S., Beckmann, F., Herzen, J., Brunke, O., Salmon, P., Friess, S., Laib, A., Koller, B., Hemberger, T., Müller-Gerbl, M., and Müller, B., "Comparative micro computed tomography study of a vertebral body," Proc. SPIE 7078, 70780C (2008).

[17] Bidola, P., Morgan, K., Willner, M., Fehringer, A., Allner, S., Prade, F., Pfeiffer, F., and Achterhold, K., "Application of sensitive, high-resolution imaging at a commercial lab-based X-ray micro-CT system using propagation-based phase retrieval," Journal of Microscopy 266(2), 211-220 (2017).

[18] Krenkel, M., Töpperwien, M., Dullin, C., Alves, F., and Salditt, T., "Propagation-based phase-contrast tomography for high-resolution lung imaging with laboratory sources," AIP Advances 6(3), 035007 (2016).

[19] Töpperwien, M., Krenkel, M., Vincenz, D., Stöber, F., Oelschlegel, A. M., Goldschmidt, J., and Salditt, T., "Three-dimensional mouse brain cytoarchitecture revealed by laboratory-based x-ray phase-contrast tomography," Scientific Reports 7, 42847 (2017).

[20] Bosshardt, D. D., and Selvig, K. A., "Dental cementum: the dynamic tissue covering of the root," Periodontology 2000 13(1), 41-75 (1997).

[21] Yamamoto, T., Hasegawa, T., Yamamoto, T., Hongo, H., and Amizuka, N., "Histology of human cementum: Its structure, function, and development," Japanese Dental Science Review 52(3), 63-74 (2016).

[22] Mani-Caplazi, G., Hotz, G., Wittwer-Backofen, U., and Vach, W., "Measuring incremental line width and appearance in the tooth cementum of recent and archaeological human teeth to identify irregularities: First insights using a standardized protocol," International Journal of Paleopathology 27, 24-37 (2019).

[23] Tanner, C., Rodgers, G., Schulz, G., Osterwalder, M., Mani-Caplazi, G., Hotz, G., Scheel, M., Weitkamp, T., and Müller, B., "Extended-field synchrotron microtomography for non-destructive analysis of incremental lines in archeological human teeth cementum," Proc. SPIE 11840, 1184019 (2021).

[24] Naji, S., Colard, T., Blondiaux, J., Bertrand, B., d'Incau, E., and Bocquet-Appel, J.-P., "Cementochronology, to cut or not to cut?," International Journal of Paleopathology 15, 113-119 (2016).

[25] Lieberman, D. E., "Life history variables preserved in dental cementum microstructure," Science 261(5125), 1162-1164 (1993).

[26] Colard, T., Bertrand, B., Naji, S., Delannoy, Y., and Bécart, A., "Toward the adoption of cementochronology in forensic context," International Journal of Legal Medicine 132(4), 1117-1124 (2018).

[27] Cerrito, P., Bailey, S. E., Hu, B., and Bromage, T. G., "Parturitions, menopause and other physiological stressors are recorded in dental cementum microstructure," Scientific Reports 10, 5381 (2020).

[28] Bertrand, B., Cunha, E., Bécart, A., Gosset, D., and Hédouin, V., "Age at death estimation by cementochronology: Too precise to be true or too precise to be accurate?," American Journal of Physical Anthropology 169(3), 464-481 (2019).

[29] Le Cabec, A., Tang, N. K., Ruano Rubio, V., and Hillson, S., "Nondestructive adult age at death estimation: visualizing cementum annulations in a known age historical human assemblage using synchrotron X-ray microtomography," American Journal of Physical Anthropology 168(1), 25-44 (2019).

[30] Howe, K., Clark, M. D., Torroja, C. F., Torrance, J., Berthelot, C., Muffato, M., Collins, J. E., Humphray, S., McLaren, K., and Matthews, L., "The zebrafish reference genome sequence and its relationship to the human genome," Nature 496(7446), 498-503 (2013).

[31] McCampbell, K. K., and Wingert, R. A., "New tides: using zebrafish to study renal regeneration," Translational Research 163(2), 109-122 (2014).

[32] White, R. M., Sessa, A., Burke, C., Bowman, T., LeBlanc, J., Ceol, C., Bourque, C., Dovey, M., Goessling, W., Burns, C. E., and Zon, L. I., "Transparent adult zebrafish as a tool for in vivo transplantation analysis," Cell Stem Cell 2(2), 183-189 (2008).

[33] Babaei, F., Hong, T. L. C., Yeung, K., Cheng, S. H., and Lam, Y. W., "Contrast-enhanced X-ray micro-computed tomography as a versatile method for anatomical studies of adult zebrafish," Zebrafish 13(4), 310-316 (2016).

[34] Vågberg, W., Larsson, D. H., Li, M., Arner, A., and Hertz, H. M., "X-ray phase-contrast tomography for high-spatial-resolution zebrafish muscle imaging," Scientific Reports 5, 16625 (2015).

[35] Cörek, E., Rodgers, G., Siegrist, S., Einfalt, T., Detampel, P., Schlepütz, C. M., Sieber, S., Fluder, P., Schulz, G., Unterweger, H., Alexiou, C., Müller, B., Puchkov, M., and Huwyler, J., "Shedding light on metal-based nanoparticles in zebrafish by computed tomography with micrometer resolution," Small 16(31), 2000746 (2020).

[36] Ding, Y., Vanselow, D. J., Yakovlev, M. A., Katz, S. R., Lin, A. Y., Clark, D. P., Vargas, P., Xin, X., Copper, J. E., Canfield, V. A., Ang, K. C., Wang, Y., Xiao, X., De Carlo, F., van Rossum, D. B., La Riviere, P., and Cheng, K. C., "Computational 3D histological phenotyping of whole zebrafish by X-ray histotomography," Elife 8, (2019).

[37] Osterwalder, M., Bolten, J. S., Rodgers, G., Humbel, M., Schulz, G., Tanner, C., Huwyler, J., and Müller, B., "Hard X-ray microtomography of Zebrafish larvae," Proc. SPIE 11886, 1188614 (2021).

[38] Lee, S. K., and Wolfe, S. W., "Peripheral nerve injury and repair," Journal of the American Academy of Orthopaedic Surgeons 8(4), 243-252 (2000).

[39] Pan, D., Mackinnon, S. E., and Wood, M. D., "Advances in the repair of segmental nerve injuries and trends in reconstruction," Muscle & Nerve 61(6), 726-739 (2020).

[40] Lubetzki, C., Zalc, B., Williams, A., Stadelmann, C., and Stankoff, B., "Remyelination in multiple sclerosis: from basic science to clinical translation," The Lancet Neurology 19(8), 678-688 (2020).

[41] Gross, W., Trabandt, A., and Reinhold-Keller, E., "Diagnosis and evaluation of vasculitis," Rheumatology 39(3), 245-252 (2000).

[42] Bikis, C., Degrugillier, L., Thalmann, P., Schulz, G., Müller, B., Hieber, S. E., Kalbermatten, D. F., and Madduri, S., "Three-dimensional imaging and analysis of entire peripheral nerves after repair and reconstruction," Journal of Neuroscience Methods 295, 37-44 (2018).

[43] Töpperwien, M., Krenkel, M., Ruhwedel, T., Möbius, W., Pacureanu, A., Cloetens, P., and Salditt, T., "Phase-contrast tomography of sciatic nerves: image quality and experimental parameters," Journal of Physics: Conference Series 849, 012001 (2017).

[44] Bartels, M., Krenkel, M., Cloetens, P., Möbius, W., and Salditt, T., "Myelinated mouse nerves studied by X-ray phase contrast zoom tomography," Journal of Structural Biology 192(3), 561-568 (2015).

[45] Hopkins, T. M., Heilman, A. M., Liggett, J. A., LaSance, K., Little, K. J., Hom, D. B., Minteer, D. M., Marra, K. G., and Pixley, S. K., "Combining micro-computed tomography with histology to analyze biomedical implants for peripheral nerve repair," Journal of Neuroscience Methods 255, 122-130 (2015).

[46] Lewis, J. R., "The system usability scale: past, present, and future," International Journal of Human–Computer Interaction 34(7), 577-590 (2018).

[47] Kumar, A. A., Burgard, M., Stacey, S., Sandaradura, I., Lai, T., Coorey, C., Cincunegui, M., Staatz, C. E., and Hennig, S., "An evaluation of the user-friendliness of Bayesian forecasting programs in a clinical setting," British Journal of Clinical Pharmacology 85(10), 2436-2441 (2019).

[48] Gonzalez-Bermejo, J., Laplanche, V., Husseini, F., Duguet, A., Derenne, J., and Similowski, T., "Evaluation of the user-friendliness of 11 home mechanical ventilators," European Respiratory Journal 27(6), 1236-1243 (2006).

[49] Salmon, P., Liu, X., and Sasov, A., "A post-scan method for correcting artefacts of slow geometry changes during micro-tomographic scans," Journal of X-ray Science and Technology 17(2), 161-174 (2009).

[50] Feldkamp, L. A., Davis, L. C., and Kress, J. W., "Practical cone-beam algorithm," Journal of the Optical Society of America A 1(6), 612-619 (1984).

[51] Paganin, D. M., and Gureyev, T. E., "Phase contrast, phase retrieval and aberration balancing in shift-invariant linear imaging systems," Optics Communications 281(5), 965-981 (2008).

[52] Paganin, D., Mayo, S. C., Gureyev, T. E., Miller, P. R., and Wilkins, S. W., "Simultaneous phase and amplitude extraction from a single defocused image of a homogeneous object," Journal of Microscopy 206(1), 33-40 (2002).

[53] Stampanoni, M., Groso, A., Isenegger, A., Mikuljan, G., Chen, Q., Bertrand, A., Henein, S., Betemps, R., Frommherz, U., Böhler, P., Meister, D., Lange, M., and Abela, R., "Trends in synchrotron-based tomographic imaging: the SLS experience," Proc. SPIE 6318, 63180M (2006).

[54] Marone, F., and Stampanoni, M., "Regridding reconstruction algorithm for real-time tomographic imaging," Journal of Synchrotron Radiation 19(6), 1029-1037 (2012).

[55] Weitkamp, T., Scheel, M., Giorgetta, J., Joyet, V., Le Roux, V., Cauchon, G., Moreno, T., Polack, F., Thompson, A., and Samama, J., "The tomography beamline ANATOMIX at Synchrotron SOLEIL," Journal of Physics: Conference Series 849, 012037 (2017).

[56] Rodgers, G., Schulz, G., Deyhle, H., Kuo, W., Rau, C., Weitkamp, T., and Müller, B., "Optimizing contrast and spatial resolution in hard x-ray tomography of medically relevant tissues," Applied Physics Letters 116(2), 023702 (2020).

[57] Yushkevich, P. A., Piven, J., Hazlett, H. C., Smith, R. G., Ho, S., Gee, J. C., and Gerig, G., "User-guided 3D active contour segmentation of anatomical structures: Significantly improved efficiency and reliability," NeuroImage 31(3), 1116-1128 (2006).

[58] Klein, S., Staring, M., Murphy, K., Viergever, M. A., and Pluim, J. P., "elastix: A toolbox for intensity-based medical image registration," IEEE Transactions on Medical Imaging 29(1), 196-205 (2009).

[59] Shamonin, D. P., Bron, E. E., Lelieveldt, B. P., Smits, M., Klein, S., and Staring, M., "Fast parallel image registration on CPU and GPU for diagnostic classification of Alzheimer's disease," Frontiers in Neuroinformatics 7, 50 (2014).

[60] Lehmann, T. M., Gonner, C., and Spitzer, K., "Addendum: B-spline interpolation in medical image processing," IEEE Transactions on Medical Imaging 20(7), 660-665 (2001).

[61] Burrell, J. C., Browne, K. D., Dutton, J. L., Laimo, F. A., Das, S., Brown, D. P., Roberts, S., Petrov, D., Ali, Z., Ledebur, H. C., Rosen, J. M., Kaplan, H. M., Wolf, J. A., Smith, D. H., Chen, H. I., and Cullen, D. K., "A porcine model of peripheral nerve injury enabling ultra-long regenerative distances: surgical approach, recovery kinetics, and clinical relevance," Neurosurgery 87(4), 833-846 (2020).

[62] Cheng, K. C., "A life-span atlas for the zebrafish," Zebrafish 1(2), 69-69 (2004).

[63] Mizutani, R., Saiga, R., Takekoshi, S., Inomoto, C., Nakamura, N., Itokawa, M., Arai, M., Oshima, K., Takeuchi, A., Uesugi, K., Terada, Y., and Suzuki, Y., "A method for estimating spatial resolution of real image in the Fourier domain," Journal of Microscopy 261(1), 57-66 (2016).

[64] Vescovi, R., Du, M., Andrade, V. d., Scullin, W., Gürsoy, D., and Jacobsen, C., "Tomosaic: efficient acquisition and reconstruction of teravoxel tomography data using limited-size synchrotron X-ray beams," Journal of Synchrotron Radiation 25(5), 1478-1489 (2018).

[65] Modregger, P., Lübbert, D., Schäfer, P., and Köhler, R., "Spatial resolution in Bragg-magnified X-ray images as determined by Fourier analysis," Physica Status Solidi (a) 204(8), 2746-2752 (2007).

[66] Tuohimaa, T., Otendal, M., and Hertz, H. M., "Phase-contrast x-ray imaging with a liquid-metal-jet-anode microfocus source," Applied Physics Letters 91(7), 074104 (2007).

[67] Santos, R., Ursu, O., Gaulton, A., Bento, A. P., Donadi, R. S., Bologa, C. G., Karlsson, A., Al-Lazikani, B., Hersey, A., Oprea, T. I., and Overington, J. P., "A comprehensive map of molecular drug targets," Nature Reviews Drug Discovery 16(1), 19-34 (2017).

[68] Newham, E., Gill, P. G., Brown, K. R., Gostling, N. J., Corfe, I. J., and Schneider, P., "A robust, semi-automated approach for counting cementum increments imaged with X-ray computed tomography," bioRxiv, (2021).

[69] Heimel, P., Swiadek, N. V., Slezak, P., Kerbl, M., Schneider, C., Nürnberger, S., Redl, H., Teuschl, A. H., and Hercher, D., "Iodine-enhanced micro-CT imaging of soft tissue on the example of peripheral nerve regeneration," Contrast Media & Molecular Imaging 2019, (2019).

[70] Diamantopoulos, A. P., Haugeberg, G., Lindland, A., and Myklebust, G., "The fast-track ultrasound clinic for early diagnosis of giant cell arteritis significantly reduces permanent visual impairment: towards a more effective strategy to improve clinical outcome in giant cell arteritis?," Rheumatology 55(1), 66-70 (2016).

[71] Cao, Y., Zhang, M., Ding, H., Chen, Z., Tang, B., Wu, T., Xiao, B., Duan, C., Ni, S., Jiang, L., Luo, Z., Li, C., Zhao, J., Liao, S., Yin, X., Fu, Y., Xiao, T., Lu, H., and Hu, J., "Synchrotron radiation micro-tomography for high-resolution neurovascular network morphology investigation," Journal of Synchrotron Radiation 26(3), 607-618 (2019).

[72] Kuan, A. T., Phelps, J. S., Thomas, L. A., Nguyen, T. M., Han, J., Chen, C.-L., Azevedo, A. W., Tuthill, J. C., Funke, J., Cloetens, P., Pacureanu, A., and Lee, W.-C. A., "Dense neuronal reconstruction through X-ray holographic nano-tomography," Nature Neuroscience 23(12), 1637-1643 (2020).

[73] Chaplin, C., "Failure mechanisms in wire ropes," Engineering failure analysis 2(1), 45-57 (1995).

[74] Stalder, A. K., Ilgenstein, B., Chicherova, N., Deyhle, H., Beckmann, F., Müller, B., and Hieber, S. E., "Combined use of micro computed tomography and histology to evaluate the regenerative capacity of bone grafting materials," International Journal of Materials Research 105(7), 679-691 (2014).

[75] Bikis, C., Rodgers, G., Deyhle, H., Thalmann, P., Hipp, A., Beckmann, F., Weitkamp, T., Theocharis, S., Rau, C., and Schulz, G., "Sensitivity comparison of absorption and grating-based phase tomography of paraffin-embedded human brain tissue," Applied Physics Letters 114(8), 083702 (2019).